RSC Advances

PAPER

View Article Online
View Journal | View Issue

Cite this: *RSC Adv.*, 2024, **14**, 20152

Disrupting redox homeostasis for tumor therapy based on PDT/chemo/ferroptosis therapeutic hybrid liposomes†

Yuanping Huang,[ac] Hongsen Liu,[cd] Yanfei Zhao,[a] Haoran Chen,[c] Qiqing Li,[c] Xiaodan Li,*[a] Shucheng Hua,*[a] Dianbo Cao*[b] and Yulei Chang[c]

Synergistic photodynamic therapy (PDT) with other therapeutic modalities can enhance the therapeutic efficacy of tumor treatment and reduce the adverse effects associated with drug leakage and off-target accumulation. However, shaping combined strategies for synergistic therapy remains challenging. Herein, we developed versatile hybrid liposomes self-assembled from Ce6–lipid conjugates and loaded with the chemo drug doxorubicin (DOX) and ferroptosis inducer Fe_3O_4 nanoparticles for synergistic PDT/chemo/ferroptosis therapy. Abundant ROS are generated by PDT upon 650 nm light irradiation, Fe_3O_4-mediated Fenton reaction, and DOX-induced apoptosis. Furthermore, amplifying oxidative stress in cancer cells to disrupt cellular redox homeostasis could accelerate tumor cell death through oxidative damage to lipids, proteins, and DNA. Overall, this work highlights liposome-based therapeutic nanoformulations, thus offering a breakthrough redox homeostasis-based synergistic PDT/chemo/ferroptosis therapy for lung cancer.

Received 7th May 2024
Accepted 9th June 2024

DOI: 10.1039/d4ra03361b

rsc.li/rsc-advances

Introduction

Photodynamic therapy (PDT) involves specific excitation wavelengths, oxygen, and photosensitizers, and non-invasive ROS-based tumor therapeutic modalities.[1–3] However, PDT as a monotherapy often suffers from incomplete tumor ablation due to limited light penetration in tissue, hypoxia induced insufficient oxygen supply in solid tumors, challenges in treating metastases, and resistance to the oxidative escape mechanism of the tumor microenvironment (*e.g.*, PDT-induced DNA damage response, which in turn upregulates glutathione peroxidase 4 (GPX4)).[4,5] To date, numerous reports have demonstrated that combined therapy holds great promise for tumor treatment.[6–8] Notably, there are multiple approaches to disrupt intracellular redox homeostasis during antitumor therapy.[9]

Intracellular redox homeostasis refers to the dynamic balance between intracellular redox substances and is vital in maintaining normal physiological processes, *e.g.*, cell growth, metabolism, differentiation, aging, and programmed death.[10,11] This redox homeostasis is also suitable for tumor cells but is maintained at a higher level. Inspired by these overexpressed oxidizing species (H_2O_2) and reducing species (GSH), tremendous efforts have been devoted to achieving controllable drug release[12–14] and redox dyshomeostasis-induced therapeutic strategies. Conversely, amplifying oxidative stress to disrupt cellular redox homeostasis could accelerate tumor cell death through oxidative damage to lipids, proteins, and DNA.[15,16]

Combining chemotherapy with PDT is an effective therapeutic strategy for redox dyshomeostasis[17,18] because many chemotherapy drugs can increase the ROS (such as H_2O_2) level in tumor cells. For instance, the FDA-approved doxorubicin (DOX) could rapidly induce oxygen into ROS, including H_2O_2, by a single-electron addition to the quinone moiety of ring C in the DOX molecule to form semiquinone.[19,20] Therefore, the combination of PDT with DOX in a nanoplatform has shown great potential for oxidative damage to tumor cells *via* ROS accumulation.

Furthermore, converting H_2O_2 into highly toxic ROS, such as hydroxyl radicals ($^{\bullet}OH$), would be a better strategy to amplify antitumor effects. Fortunately, the intracellular Fenton reaction is H_2O_2-dependent, and Fe^{2+}/Fe^{3+} mediates $^{\bullet}OH$ generation.[21,22] The Fenton or Fenton-like-based reagents were recently

[a]*Department of Respiratory Medicine, The First Hospital of Jilin University, Changchun 130021, China. E-mail: ddjy@jlu.edu.cn; hsc@jlu.edu.cn*

[b]*Department of Radiology, The First Hospital of Jilin University, Changchun 130021, China. E-mail: caodb@jlu.edu.cn*

[c]*Key Laboratory of Luminescence Science and Technology, Chinese Academy of Sciences & State Key Laboratory of Luminescence and Applications, Changchun Institute of Optics, Fine Mechanics and Physics, Chinese Academy of Sciences, Changchun 130033, Jilin, China*

[d]*Stomatology Hospital, School of Stomatology, Zhejiang University School of Medicine, Zhejiang Provincial Clinical Research Center for Oral Diseases, Key Laboratory of Oral Biomedical Research of Zhejiang Province, Cancer Center of Zhejiang University, Engineering Research Center of Oral Biomaterials and Devices of Zhejiang Province, Hangzhou 310000, China*

† Electronic supplementary information (ESI) available. See DOI: https://doi.org/10.1039/d4ra03361b

explored to boost this reaction and then induce cell apoptosis for antitumor therapy.[23,24] In addition, amplified oxide stress causes ferroptosis—a newly discovered iron-dependent, non-apoptotic, and programmed cell death pathway.[25,26] Ferroptosis is characterized by the accumulation of lipid peroxides (LPOs), the downregulation of GPX4, the vacuolation of mitochondria, and the disappearance of their ridges.[27,28] Emerging evidence suggests that related inducers could potentially trigger ferroptosis for antitumor therapy, particularly for eradicating the resistance to traditional monotherapies. Consequently, combining the PDT/chemo/ferroptosis therapeutic strategies exhibits good potential in boosting the intracellular ROS level and breaking redox homeostasis, thus significantly strengthening the antitumor effect.

Herein, we developed Ce6–lipid stabilized DOX and Fe_3O_4 nanoparticle (NP)-based hybrid liposomes for PDT/chemo/ferroptosis synergistic tumor therapy. Synthetic Ce6–lipid, as one of the backbones of liposomes, could effectively prevent the release of Ce6 from hybrid liposomes and avoid the decrease in single oxygen efficiency caused by Ce6 aggregation. The released DOX molecules could anchor the DNA pairs, inducing cell apoptosis and increasing intracellular ROS. Subsequently, Fe_3O_4 NPs could release ferrous ions under acidic TME and convert a high level of H_2O_2 into $^{\bullet}OH$ to induce ferroptosis. This study provides a promising synergistic strategy for regulating cellular redox homeostasis and enhancing the therapeutic efficacy of lung cancer (Scheme 1).

Results and discussion

Liposome characterization

To synthesize Ce6–lipid stabilized DOX and Fe_3O_4 hybrid liposomes, various components, including Ce6–lipid and water-soluble Fe_3O_4, were prepared. Briefly, the photosensitizer Ce6 was conjugated to the lyso-PC to form a Ce6–lipid molecule *via* the ester linkages, and its chemical structure was confirmed by ^{1}H NMR (Fig. S1a†). It could be incorporated into liposomes as a framework through self-assembly due to the hydrophobic

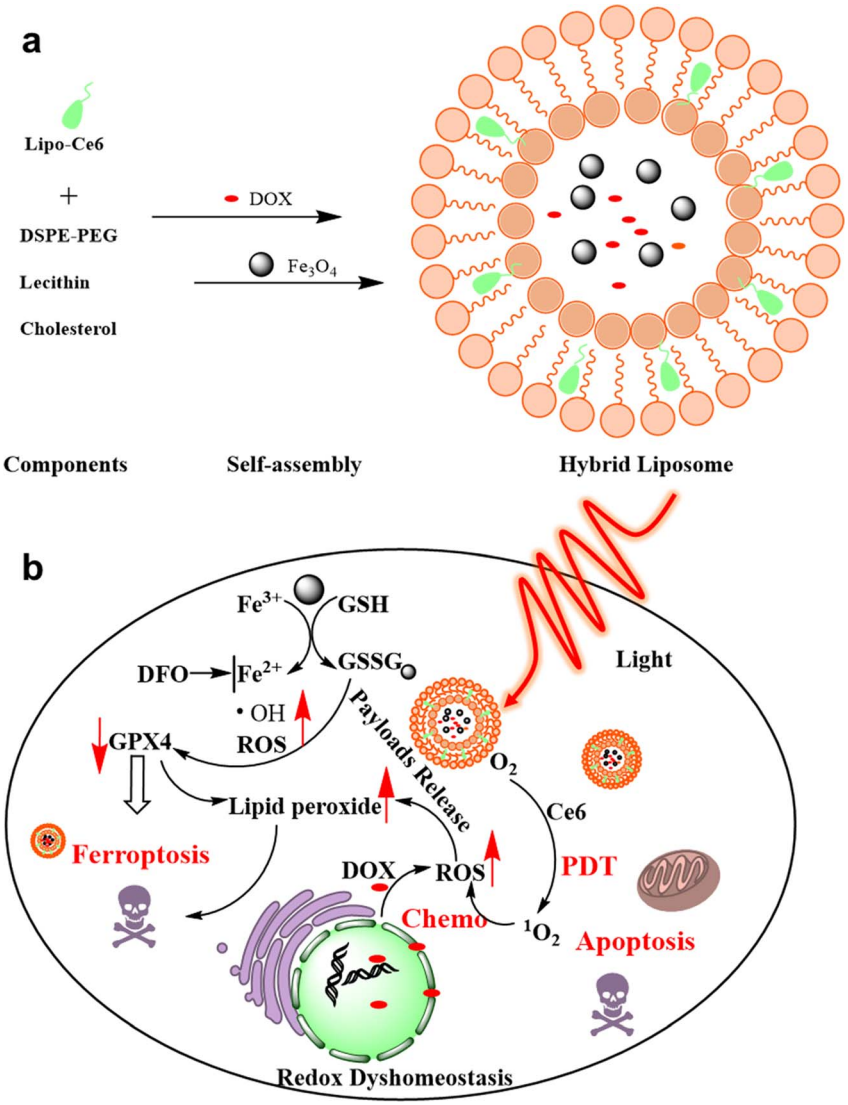

Scheme 1 Schematic representation of (a) the hybrid liposomes and (b) their ROS dyshomeostasis mechanism of antitumor action.

nature of Ce6–lipid. The as-obtained Lipo-Ce6 liposomes could be excited by a specific laser to perform PDT. Thus, to obtain the optimal doping ratio of Ce6–lipid, various Ce6–lipid-based (Lipo-Ce6) liposomes were prepared *via* thin film hydration. Dynamic light scattering (DLS) results in Fig. S1b† show that a similar size (~130 nm) and narrow PDI of Lipo-Ce6 liposomes could be detected among the different doping levels of Ce6–lipid. Because cytotoxic singlet oxygen yield is critical for PDT, the singlet oxygen production profiles of the Ce6–lipid-based liposomes were evaluated using a DPBF probe. As shown in Fig. S1c,† with the increase in irradiation time, the absorption spectra intensity of DPBF at 417 nm gradually decreases upon 650 nm light irradiation, indicating that the resulting singlet oxygen consumed the DPBF molecules. A Ce6–lipid content higher than 9% cannot further increase the singlet oxygen yield, implying that aggregation-induced quenching occurs. Thus, the optimal amount of Ce6–lipid is 9% (w/w, Ce6 ≈ 5%). Next, to prepare the Lipo@Fe_3O_4 liposomes, a similar film hydration method was performed using the aqueous Fe_3O_4 NP solution. Before that, the aqueous soluble Fe_3O_4 NPs were obtained using the $NOBF_4$-treated method[29] to remove the surface-capped oleic acid ligands of Fe_3O_4 NPs. After centrifugation, the Fe_3O_4 NPs were transferred from the oil phase (cyclohexane) to the aqueous solution. Afterward, a chemotherapeutic agent (DOX) was loaded into the Lipo-Ce6 liposomes using an $(NH_4)_2SO_4$ gradient method[30] to prepare Lipo-Ce6@DOX liposomes. Subsequently, the Lipo-Ce6@Fe_3O_4–DOX hybrid liposomes were prepared by applying a successive hydration process.

Furthermore, successful encapsulation was confirmed by transmission electron microscopy (TEM) assay. It can be observed that the Fe_3O_4 NPs were packed within the liposomes with high contrast (Fig. 1a). The encapsulation of DOX was further confirmed by comparing UV-Vis absorption spectra before and after introducing the DOX solution (Fig. 1b), and the drug loading efficiency (DLE) of DOX is 70%, where DLE = (weight of loaded drug/weight of input drug) × 100%, drug loading capacity (DLC) is 9.2%, and DLC = (weight of loaded drug/weight of polymer + drug used) × 100%. Those loaded solely with DOX (Lipo-DOX) and Lipo@Fe_3O_4 liposomes were also studied by DLS with 106.6 ± 3.48 nm and 110.06 ± 5.2 nm, along with zeta potentials of −3.2 mV and −9.08 mV, respectively (Fig. 1c and d). These results confirm the successful preparation of various liposomes.

Evaluation of payload release profiles and singlet oxygen detection

To investigate the DOX release profiles, hybrid liposomes of Lipo-Ce6@Fe_3O_4–DOX were performed in a pH 7.4 buffer medium. The cumulative drug release properties in Fig. 1e demonstrated the DOX-released profiles from the hybrid liposomes within 24 h. A rapid release of DOX was observed in the first 4 h. Then, the DOX release rate decreased, and the cumulative release rate was ~63%. To avoid the decrease in singlet oxygen efficiency caused by the aggregation of free Ce6 molecules, similarly, we further studied the Ce6 release profiles. Fortunately, unlike DOX, no noticeable characteristic Ce6 absorption spectrum was detected at around 650 nm, indicating that Ce6–lipid molecules were stable in the matrix and not released from hybrid liposomes under the same conditions because they were anchored in the liposome skeleton (Fig. S2†). These results suggest that the hybrid liposomes could maintain stable singlet oxygen efficiency upon 650 nm irradiation. Next, DPBF molecules were employed as a singlet oxygen probe to

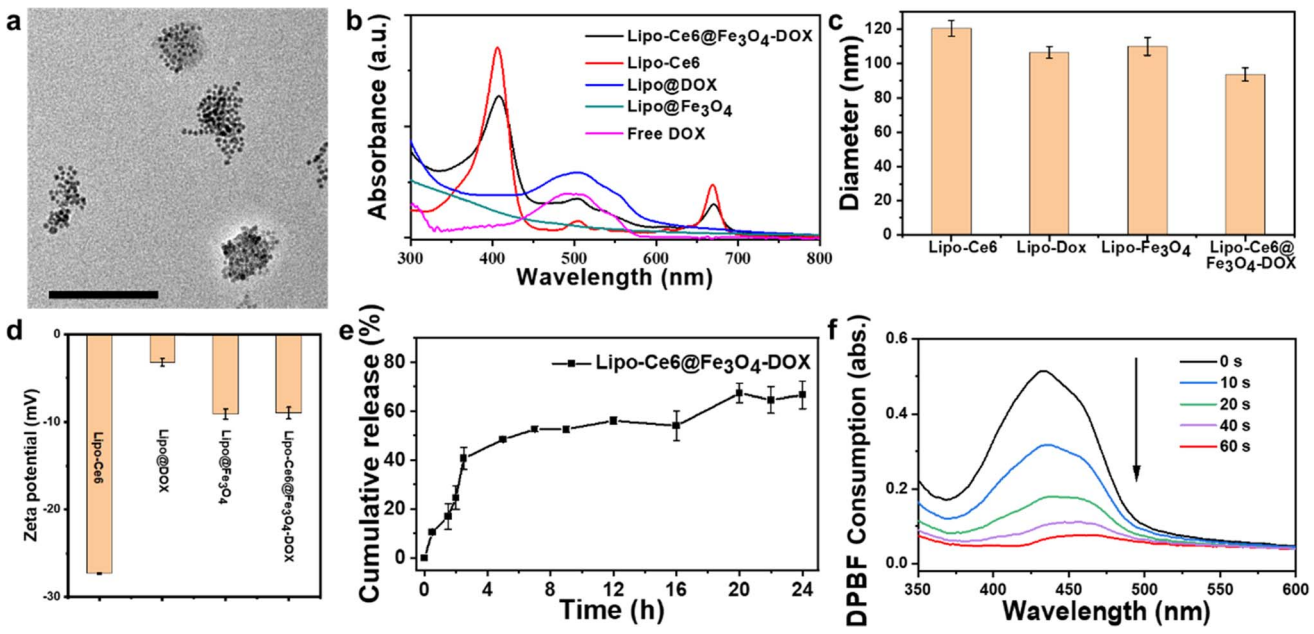

Fig. 1 (a) TEM image of hybrid liposomes, scale bar: 200 nm. (b) UV-vis spectra of liposomes (Lipo-Ce6@Fe_3O_4–DOX, Lipo-Ce6, Lipo@DOX and Lipo@Fe_3O_4) and free DOX. (c) Hydrodynamic diameter and (d) zeta potential of various liposomes (Lipo-Ce6, Lipo@DOX, Lipo@Fe_3O_4, and Lipo-Ce6@Fe_3O_4). (e) Payload release profiles. (f) ROS generation of hybrid liposomes after 650 nm light irradiation with DPBF as a probe.

evaluate the singlet oxygen generation level. As shown in Fig. 1f, after increasing the light exposure time upon 650 nm excitation, the decreased DPBF absorbance at 417 nm indicates effective singlet oxygen generation.

Cellular uptake and *in vitro* antitumor effects

The endocytosis behavior of Lipo-Ce6@ Fe_3O_4–DOX hybrid liposome was then studied in A549 cells, significantly influencing the phototherapy effects. Fluorescence microscopy was used to evaluate intracellular uptake. The red emission of Ce6 was observed around the nuclei stained by DAPI (blue emission) and within the cell membrane stained by DiO over time (the relative intensity from 1 to 30 min is 15.06, 128.03, and 106.65%, quantitative statistics, as shown in Fig. S3,† indicating that the hybrid liposomes were efficiently taken up in A549 cells within 10 min of incubation (Fig. 2)).

Next, hybrid liposome-mediated PDT/chemo/ferroptosis synergistic antitumor effects were studied. The CCK8 assay was used to assess the combined therapy effects after various nanoformulations of liposome treatment (Fig. 3). To better demonstrate the therapeutic effects of different treatment methods, the PDT effect related to light dose (time-dependent) was first studied. After the treatment of Lipo-Ce6 liposomes under 650 nm light irradiation (100 mW cm^{-2}), the relationship between exposure time and cytotoxicity is shown in Fig. 3a. Cell viability declined rapidly when A549 cells were exposed to the 650 nm light. The cell viability was about 50% after 20 s of irradiation and significantly decreased upon 40 s of irradiation. After confirming the PDT effects *in vitro*, we further evaluated the dose-dependent effect of DOX and Fe_3O_4 on cell viability in Lipo@DOX and Lipo@Fe_3O_4 liposomes, respectively. With encapsulated DOX over 24 h incubation, only slight cytotoxicity was observed. However, obvious cytotoxicity was observed with free DOX at the same concentration (Fig. S4a†), as it has higher bioavailability and can diffuse freely into cells compared to the DOX encapsulated and retained in liposomes.[31] In addition, a dose-dependent manner of Lipo@Fe_3O_4 liposomes showed that cell viability decreased to 47.5% at 400 μg mL^{-1}, exhibiting slightly stronger toxicity than Fe_3O_4 simultaneously (Fig. S4b†). Therefore, the dose-dependent Lipo-Ce6@Fe_3O_4–DOX liposomes (determined by Ce6 concentration) with or without 650 nm light irradiation (100 mW cm^{-2}, 40 s) were investigated. As shown in Fig. 3d, the combined treatment group shows a synergistic effect compared to Lipo-Ce6 + Light and Lipo-Ce6@Fe_3O_4–DOX without light groups. The combination index (CI) was further calculated between PDT and Fe_3O_4/DOX (CI < 1.0) according to Chou and Talalay's principle,[32,33] namely, lower doses achieved greater antitumor effects, indicating better efficacy of Lipo-Ce6@Fe_3O_4–DOX liposomes in inducing cell damage. Flow cytometry with annexin V-FITC and PI staining supported the cellular killing mechanism. As shown in Fig. 3e, the Lipo-Ce6 induced an early apoptosis rate of up to 36.4% compared to the PBS control group. After treatment with Lipo-Ce6@Fe_3O_4–DOX under the same irradiation conditions, the introduction of DOX/Fe_3O_4 further increased cell apoptosis, suggesting that PDT and DOX-induced apoptosis achieved significant therapeutic efficacy because Fe_3O_4 was mainly a ferroptosis inducer.

To further investigate the PDT-induced cell damage mechanism *in vitro*, the Ce6-treated cells were irradiated with 650 nm light for RNAseq analysis. We performed RNA-seq analyses on wt and ROS (Ce6-mediated $^1O_2$)-treated cells. There was a total of 1124 differentially regulated genes (fold change >2, *p*-value ≤ 0.01), of which 622 genes were up-regulated, and 502

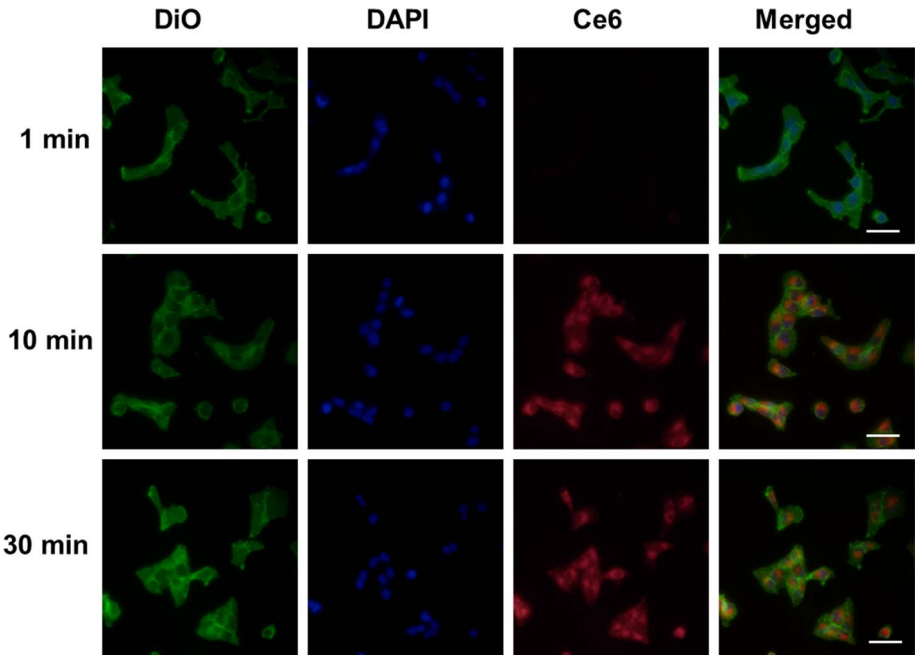

Fig. 2 Intracellular uptake profile of hybrid liposomes at different times. Scale bar = 50 μm. Corresponding quantitative statistics are shown in Fig. S3.†

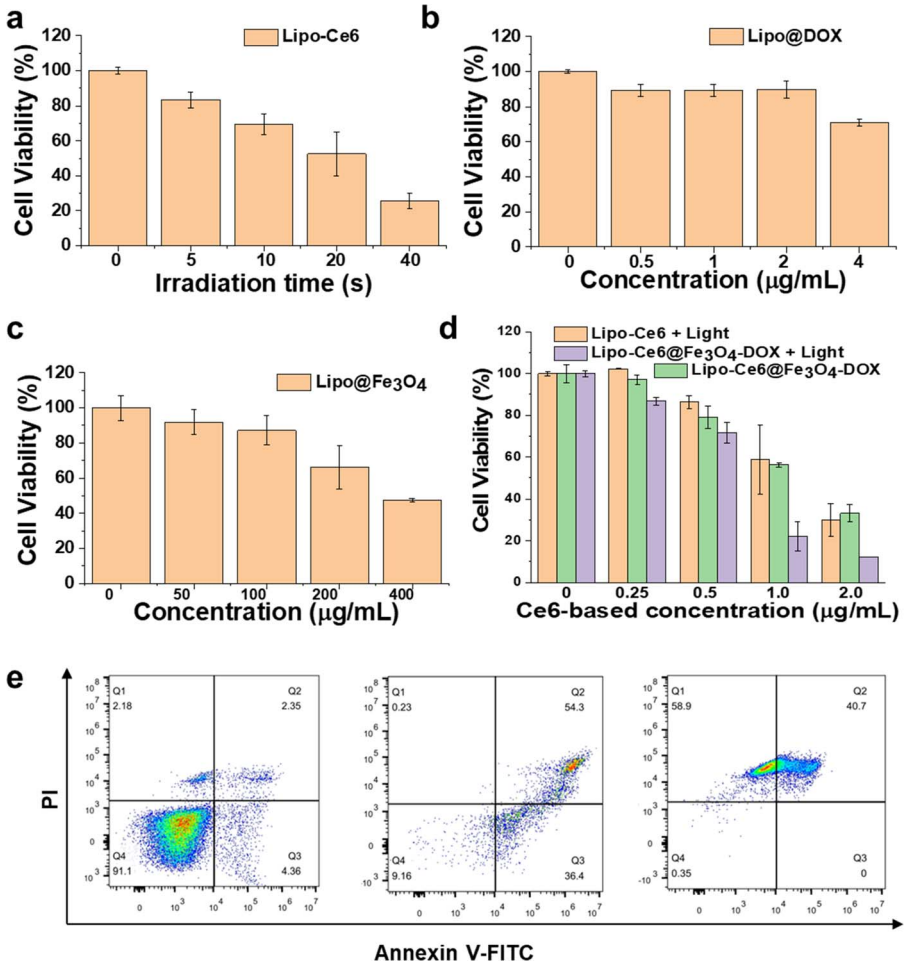

Fig. 3 Cell viability of A549 cells after treatment with (a) Lipo-Ce6 at 1.5 μg mL^{-1} and exposure to 650 nm light over time; (b) Lipo@DOX at various concentrations (0, 0.5, 1, 2 and 4 μg mL^{-1}); (c) Lipo@Fe_3O_4 at various concentrations (0, 50, 100, 200 and 400 μg mL^{-1}); (d) Ce6-based liposomes at various concentrations (0, 0.25, 0.5, 1.0 and 2.0 μg mL^{-1}) and (e) apoptosis analysis of A549 cells after different treatments (PBS, Lipo-Ce6 and Lipo-Ce6@Fe_3O_4–DOX), followed by staining with annexin V/PI and analysis using flow cytometry.

genes were down-regulated upon PDT treatment (Fig. 4a). The number of genes changing is summarized, as presented in Table 1 of ESI.†

As shown in Fig. 4b, gene pathway analyses for the upregulated genes showed that they were enriched for pathways, such as protein processing in the endoplasmic reticulum and ferroptosis. The enriched gene pathways for the downregulated genes almost exclusively involve metabolic processes, such as folate biosynthesis and phenylalanine metabolism. In addition, it shows that PDT can regulate the ferroptosis process through up-regulated related genes (Fig. 4c). Furthermore, as shown in Fig. 4d, a significant subset of ferroptosis genes, including PTGS2 and ACSL4, was dysregulated in PDT-treated cells, suggesting that ROS-mediated transcriptome changes carry some lipid metabolism of ferroptosis.

In addition, to boost the ferroptosis of A549 cells, the Fe_3O_4 NPs as ferroptosis inducers were employed and loaded within liposomes (Lipo-Fe_3O_4) for synergetic therapy. We used a Liperfluo probe to detect the accumulated LPO *in vitro* because LPO accumulation was considered a typical hallmark of ferroptosis. As shown in Fig. 5, no apparent green fluorescence was detected in the PBS group, while the intracellular green fluorescence intensity was enhanced after treatment with Lipo-Ce6@Fe_3O_4–DOX hybrid liposomes; particularly, when exposed to a 650 nm light, it showed further fluorescence intensity boost. Moreover, when the cells were pretreated with deferoxamine (DFO, an iron chelator), the inhibition of LPO accumulation (extremely weak green emission) confirmed the occurrence of ferroptosis. These results verified that combining hybrid liposomes and 650 nm light could induce ferroptosis in A549 cells.

Furthermore, as can be observed from Fig. 6b, the mRNA level of GPX4 demonstrated that the GPX4 expression was down-regulated over time and significantly deactivated after 3 h of incubation, indicating that ferroptosis can be evoked by Fe_3O_4-based liposome.[35] Moreover, the dose-dependent results suggested that the concentration of Fe_3O_4 over 50 μg mL^{-1} significantly deactivated the GPX4 within 6 h (Fig. 6a). As shown in Fig. S6a and b,† the western blot results further confirmed that Fe_3O_4 could induce the ferroptosis of A549 cells, which is consistent with a previous report.[23] Fig. 6c and d show the expression level of GPX4, which was down-regulated after

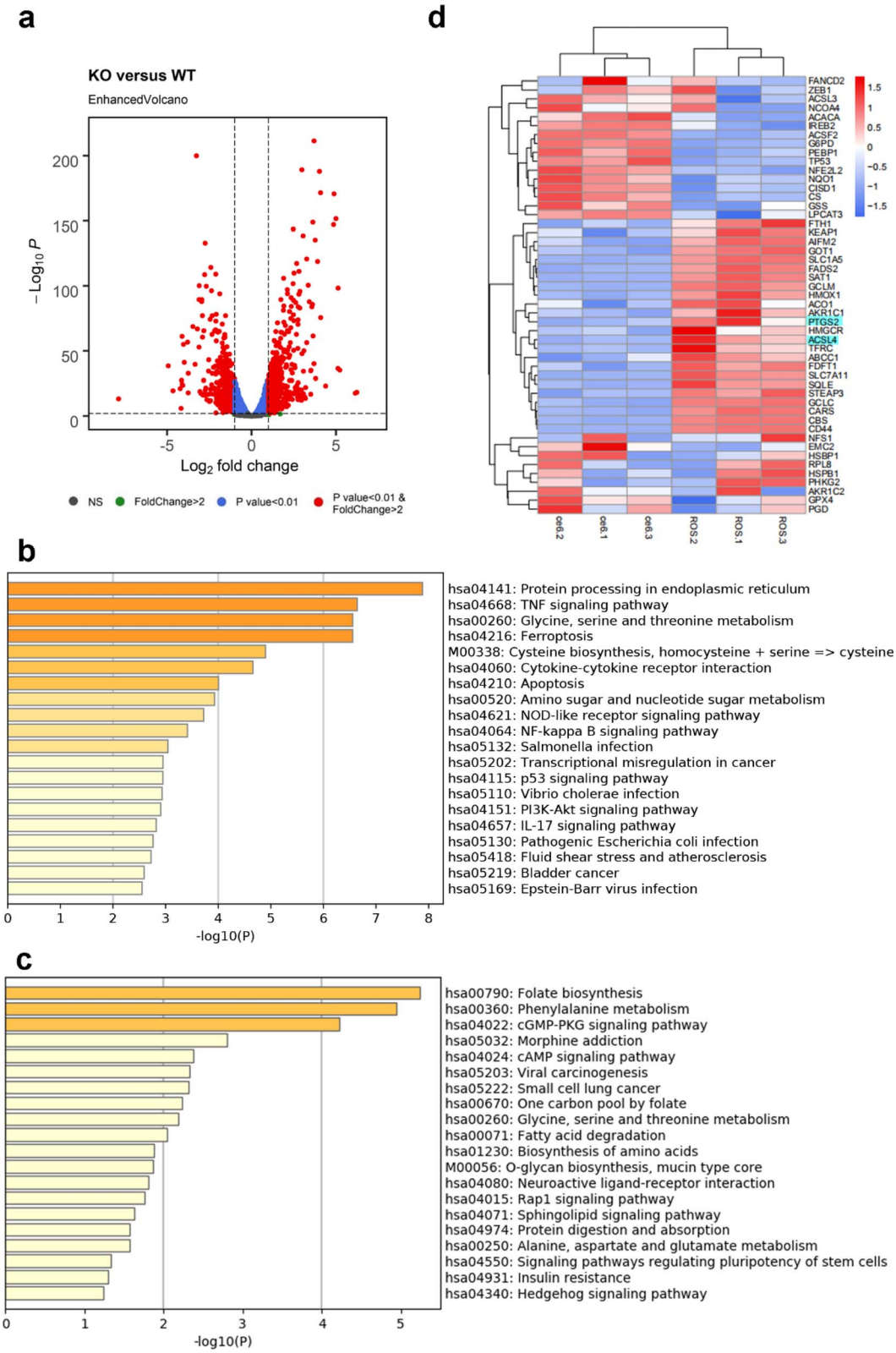

Fig. 4 (a) Volcano plot of genes differentially expressed in ROS compared to WT. Red dots represent genes with a log2 fold change of >±1 and *p*-value of ≤0.01. Functional annotation analysis of differentially expressed genes using metascape.[34] (b) KEGG analysis of upregulated gene pathways. (c) KEGG analysis of downregulated gene pathways. (d) Heatmap of expression of representative ferroptosis genes after PDT.

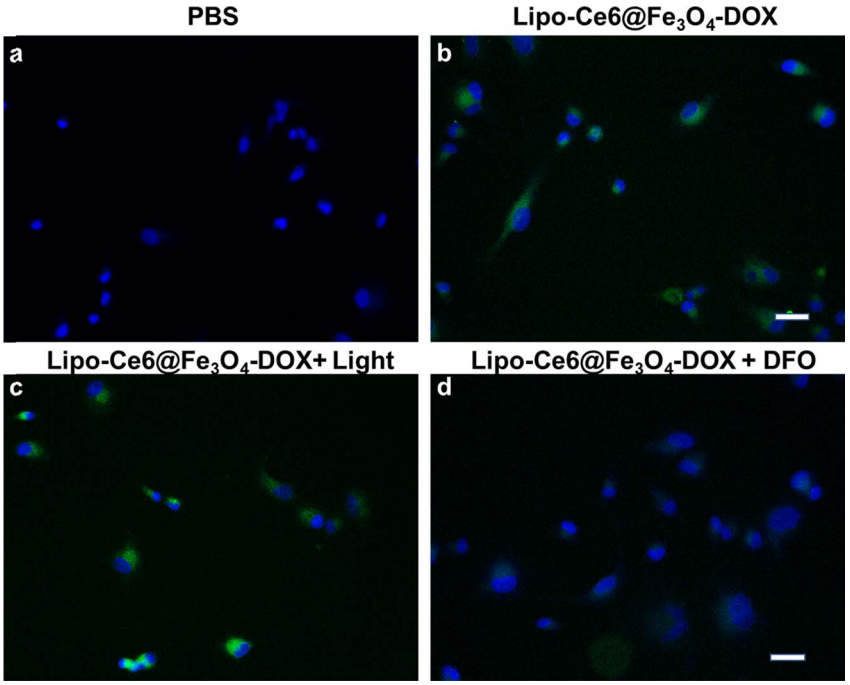

Fig. 5 Detection of intracellular LPO of A549 cells after various treatments. (a) PBS, (b) Lipo-Ce6@Fe_3O_4–DOX, (c) Lipo-Ce6@Fe_3O_4–DOX and (d) pretreated with DFO. Scale bar: 100 μm. The corresponding quantitative statistics are shown in Fig. S5.†

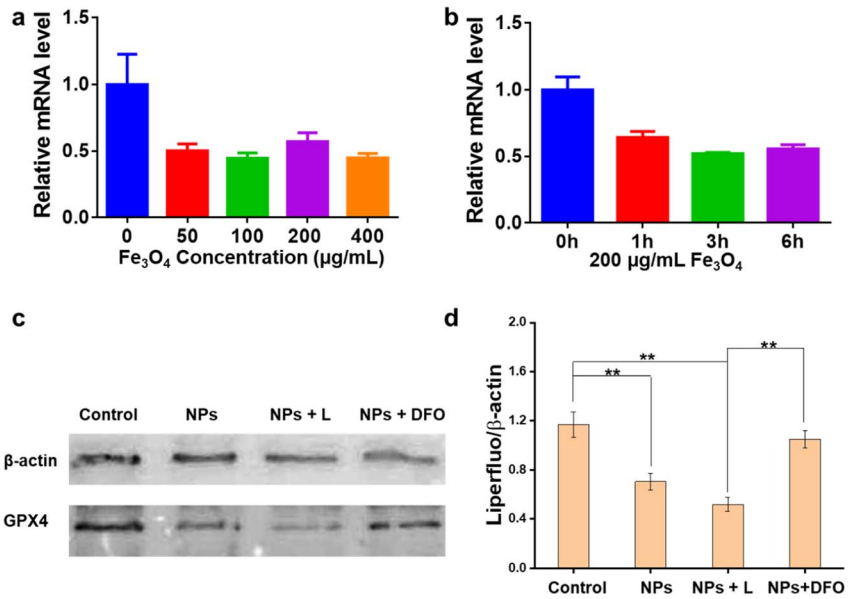

Fig. 6 (a) Dose dependence of Fe_3O_4 on the mRNA level of GPX4. (b) Time-dependent mRNA level after treatment with 200 μg mL^{-1} of Fe_3O_4. (c) Western blot analysis and relative expression of GPX4 after treatment with Lipo-Ce6@Fe_3O_4–DOX hybrid liposomes (NPs), hybrid liposome + light (NPs + L) and hybrid liposome + DFO (NPs + DFO), and (d) corresponding quantified proteins. $n = 3$.

treatment with Lipo-Ce6@Fe_3O_4–DOX NPs. After PDT treatment, GPX4 expression was further suppressed because of enhanced ROS production.

In vivo antitumor effects

Next, the antitumor efficacy *in vivo* was evaluated in Lewis lung carcinoma (LLC) tumor-bearing mice. Different formulations were i.v. injected and treated with various methods, including PBS, 650 nm light only, hybrid liposomes, and hybrid liposomes + 650 nm light (100 mW cm^{-2} for 6 min irradiation). As shown in Fig. 7, the hybrid liposomes with or without 650 nm laser irradiation exhibited tumor growth suppression capability compared to the PBS and 650 nm light-only group (Fig. 7a), indicating the effectiveness of our synthesized hybrid liposomes

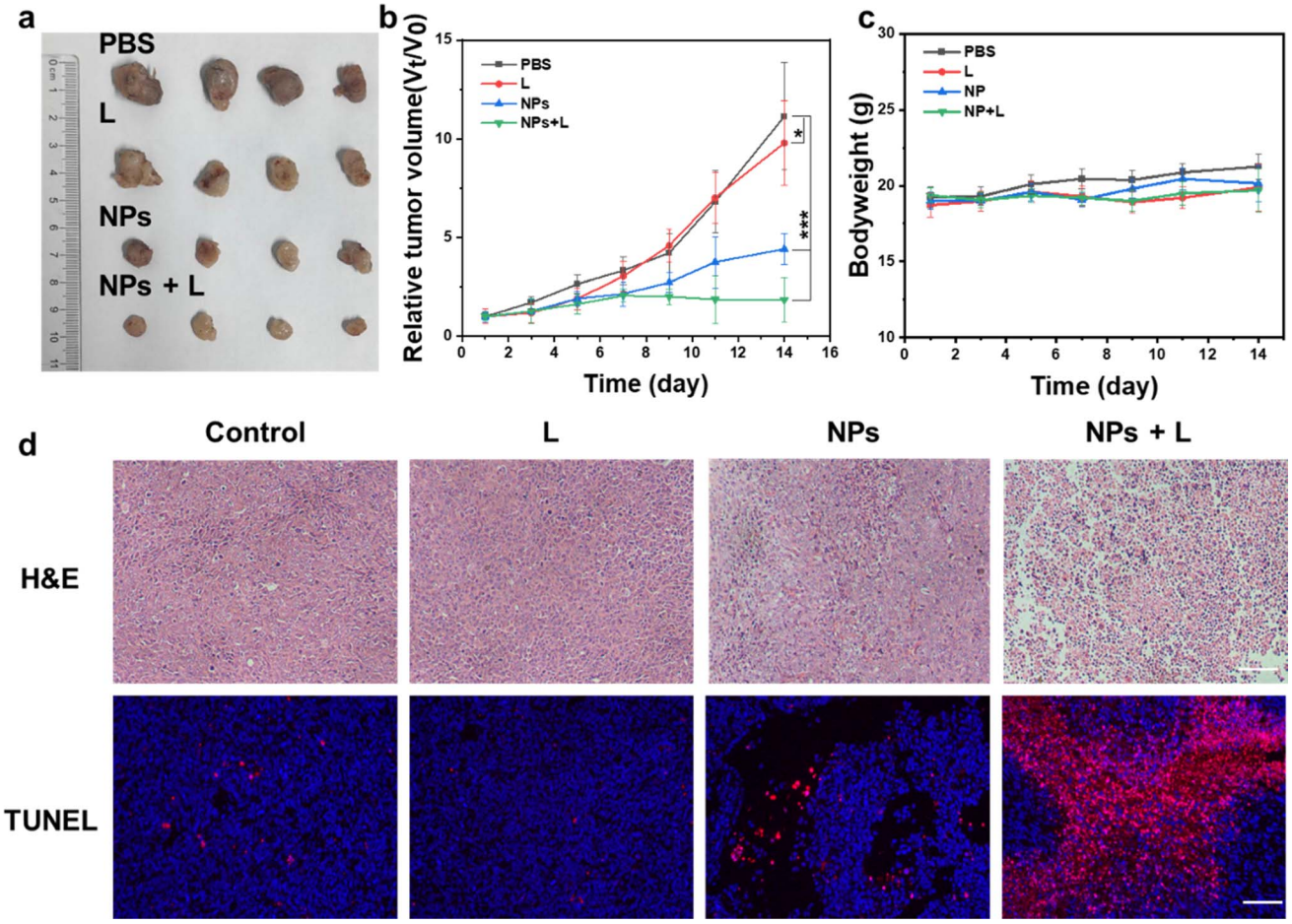

Fig. 7 *In vivo* antitumor effects of hybrid micelles. (a) Representative digital photos of tumor tissues from the different groups (PBS, 650 nm laser, Lipo-Ce6@Fe_3O_4–DOX (NPs), and Lipo-Ce6@Fe_3O_4–DOX + 650 nm laser (NPs + L)). (b) Tumor growth curves of mice after various treatments. (c) Body weight of mice after various treatments. (d) H&E and TUNEL staining images of tumor tissues from the different groups on the 14th day. Scale bar: 100 μm. The data are shown as mean ± standard deviation (s.d.) of three independent experiments, and ***$p < 0.001$ and *$p < 0.05$.

in antitumor therapy. The hybrid liposomes + 650 nm light group induced the most significant inhibition effect, evidenced by the lowest tumor growth rate (Fig. 7b) due to the synergistic light-induced PDT and chemo/ferroptosis (dark). Notably, no significant changes in the body weight of the mice were observed during the treatment (Fig. 7b). Hematoxylin and eosin (H&E) and terminal deoxynucleotidyl transferase-mediated nick end labeling (TUNEL) assays showed remarkable necrosis of tumor cells in the hybrid liposomes with a 650 nm light irradiation group, and negligible damage to normal organs was determined (Fig. S6†), suggesting the high safety of this liposome-based delivery system.

Conclusions

In summary, we developed hybrid liposomes of Lipo-Ce6@Fe_3O_4–DOX for PDT/ferroptosis/chemotherapy of tumors. The lipid-Ce6 in the framework of liposome prevents the Ce6 leakage from off-target and aggregate-induced quenching, ensuring long-term stability. The RNAseq analysis indicates that PDT could induce A549 cell apoptosis and ferroptosis, which synergize with a dose-dependent intracellular ROS inducer of DOX and a ferroptosis inducer of Fe_3O_4 NPs, showing effective cancer cell inhibition through improved ROS generation efficiency. The *in vivo* results further confirmed the effectiveness of hybrid liposomes in antitumor cancer therapy. We propose a breaking redox homeostasis strategy to address a broad spectrum of tumor therapy challenges.

Materials and methods

Preparation of liposomes

Lyso-Pc–Ce6 conjugates (Ce6–lipid) were synthesized by coupling Lyso-Pc with Ce6 molecules *via* an acylation reaction under the catalysis of EDCI and DMAP. The blank Ce6–lipid stabilized liposomes were prepared by applying thin-film hydration methods with lecithin : DSPE-PEG : cholesterol : Ce6–lipid (8.5 : 1.5 : 2 : x%, x = 1, 3, 6, 9 and 12, w/w). First, the mixture was fully dissolved in 3 mL of chloroform; then, the solvent was removed by rotary evaporation. After that, 1 mL DI-water was added to the formed film and hydrated at 45–50 °C for about 30 min to form liposomes. Similarly, the Fe_3O_4-only

liposomes with Ce6-free were prepared. The optimal ratio of Ce6–lipid in the liposome was determined by singlet oxygen yield upon 650 nm light irradiation. pH-induced hydration methods prepared the DOX-only liposomes (Ce6-free). Typically, 2 mL of NH_4SO_4 solution (123 mM) was added and hydrated at 45–50 °C for 15 min. The as-obtained Lipo@DOX was purified through a 220 nm filter, then transferred to a dialysis bag, and dialyzed against PBS buffer for 30 min. Afterward, the DOX was added to the above solution with 1 mg mL^{-1} and rehydrated for 30 min at 65 °C. The product was purified through a 220 nm filter and collected after re-dialysis. Similarly, a successive hydration approach was developed to co-encapsulate DOX and Fe_3O_4 NPs. The size and zeta potential of the formulations were characterized using Zetasizer NanoZS nanopositioners (Malvern), and their morphologies were recorded using a JEM-1200EX transmission electron microscope (JEOL, USA). Finally, the DOX-loading efficiency was measured by monitoring the absorption spectrum at 490 nm after dialysis of the hybrid liposomes.

Singlet oxygen detection

DPBF, as an indicator, was used to evaluate the singlet oxygen yield under 650 nm light irradiation in different Ce6–lipid doping levels of liposomes. Typically, 5 μL of DPBF (2 mg mL^{-1}) in ethanol was added to the various formulations and irradiated with 650 nm at 50 mW cm^{-2}. After determining the irradiation time, the DPBF consumption profiles were monitored by applying a spectrophotometer to record the absorption spectrum at 417 nm.

Payload release profiles *in vitro*

We investigated the payload release profiles from liposomes using the dialysis method.[1] Briefly, 1 mL liposomes were transferred to a dialysis bag (MW = 3500 cut-off) and immersed in a flask containing 100 mL PBS solution (pH = 7.4) under gentle stirring. Then, a 1 mL release medium containing DOX/Ce6–lipid molecules was removed at the determined time intervals, and the absorption spectrum was monitored at 490 nm or 650 nm using a spectrophotometer. The amount of DOX released from the liposomes was calculated using the following equation: release% = $C_{release}/C_{total} \times 100\%$.

Cellular experiments

Cell uptake and viability assay. A549 human lung cancer cells were cultured in a 25 mL culture flask with RPMI 1640 medium containing 10% fetal bovine serum and 1% penicillin–streptomycin for 24 h. The cells were maintained at 37 °C and 5% CO_2.

Cell viability analysis. A549 cells were incubated with various formulations for 4 h, washed twice with PBS, and subjected to 650 nm laser irradiation or no laser irradiation. A CCK8 assay was used to measure cell viability. In addition, the spectrophotometric absorbance was measured at 450 nm using a microplate reader.

Cell uptake. A549 cells were seeded in glass bottom culture dishes. Afterwards, the Ce6-based liposomes were added to the dishes after 12 h of cell adherence and further incubated for 10 min and 30 min at 37 °C and 5% CO_2, respectively. Then, the cells were fixed with 4% paraformaldehyde for 15 min, washed twice with PBS, and stained with DAPI staining solution (diluted 2000×, Beyotime, China) for 5 min and a DiO kit (1×, Beyotime, China) for 45 min. The fluorescence intensity was observed by confocal microscopy (CSi2, Nikon, Japan).

RNA-seq analysis

To examine the function of Ce6-mediated ROS ($^1O_2$) at the biological function, the Ce6-treated A549 cells with and without 650 nm light irradiation (100 mW cm^{-2} for 10 s) were tested. Total RNA from A549 cells was extracted using the RNAiso Plus (9109, Takara, Tokyo, Japan) and sent to Biomarker Technologies Co., Ltd. (Beijing, China) for RNA-seq analysis. Reads were mapped to the GRCh38 genome using HISAT2 (v2.1.0).[36] Transcripts were counted with the R package summarizeOverlaps (https://www.r-project.org/). Differential expression analysis was performed with DESeq2.[37] Genes with a false discovery rate ≤ 0.01 and a fold change ≥ 2 were selected.

Flow cytometry assay

For the flow cytometry analysis, the cells were trypsinized and stained with annexin V-FITC and propidium iodide (Annexin V-FITC Apoptosis Staining/Detection Kit) to measure the cells experiencing apoptosis. A549 cells were cultured in 6-well plates and then treated with different reagents for 4 h, and each parallel was then exposed to laser irradiation for 15 s at a density of 100 mW cm^{-2}. Cells were harvested after 24 h, washed twice with PBS, and resuspended in 50 μL of binding buffer. 5 μL of annexin-V-FITC and 5 μL of PI were added to cells and then incubated for 15 min at room temperature. 400 μL of binding buffer was added to each tube and analyzed by flow cytometry.

Western blotting

A549 cells were disrupted in RIPA lysis buffer. Protein samples were separated through SDS-PAGE and transferred to PVDF membranes for immunoblotting, and the membranes were incubated with specific antibodies targeting GPX4 and GAPDH at 4 °C overnight. Blots were incubated with the corresponding secondary antibodies for 1 h at room temperature and visualized using ECL.

In vivo antitumor therapy

All animal experiments were approved by the Institutional Ethical Committee of Animal Experimentation of the First Hospital of Jilin University, and they were performed strictly compliant with "The National Regulation of China for Care and Use of Laboratory Animals". C57BL/6 mice (6–8 weeks, ~20 g) were purchased from Liaoning Changsheng Biotechnology Company. The mice were inoculated by subcutaneous injection of LLC cells (1×10^6) into the right flank of the mice. After the tumor volumes reached ~100 mm^3, the mice were randomly divided into 4 groups (n = 5). The tumor volumes were

calculated using the formula $[(L \times W^2)/2]$, where length (L) represents the larger tumor diameter and width (W) represents the smaller one. The mice were i.v. injected with PBS (200 μL) and hybrid liposomes (200 μL, 0.108 mg mL^{-1}). After 4 h and 12 h, the 650 nm light only (200 μL PBS) and hybrid micelle groups were exposed to 650 nm light at 100 mW cm^{-2} for 6 min, respectively. Afterward, tumor growth and body weight were monitored every 2 days, and the mice were sacrificed after 14 d. The tumor and various organs (heart, liver, spleen, lung, and kidney) were excised to fix in 10% neutral buffered formalin and stained *via* hematoxylin and eosin (H&E) for pathological analysis.

Statistical analysis

All data are expressed as the mean ± standard deviation (SD), and the significance of differences among groups was evaluated with Student's *t*-test ($*p < 0.05$, $**p < 0.01$, $***p < 0.001$).

Data availability

The data supporting this article have been included as part of the ESI.†

Author contributions

Y. C. and S. H. conceived and designed the experiments. Y. H., H. L., Y. Z., H. C., Q. L. and X. L. performed the experiments. Y. H., H. L., H. C., Q. L., D. C. and Y. C. analyzed the data and prepared the manuscript. All authors contributed to manuscript writing and discussions.

Conflicts of interest

There are no conflicting interests of the authors.

Acknowledgements

This research was financially supported by the National Natural Science Foundation of China (Grant No. 62075217, 62305329), Project of Science and Technology Agency, Jilin Province (20210101148JC, 20210101289JC, 20230508104RC and 20230402039GH), Changchun Science and Technology Bureau (Grants 23GZZ06), the China Postdoctoral Science Foundation (Grants 2023M733432, 2023M741350) and Medical Special Project of Jilin Provincial Department of Finance (JLSWSRCZX2021-054).

References

1 H. Chen, F. Wu, X. Xie, W. Wang, Q. Li, L. Tu, B. Li, X. Kong and Y. Chang, Hybrid Nanoplatform: Enabling a Precise Antitumor Strategy *via* Dual-Modal Imaging-Guided Photodynamic/Chemo-/Immunosynergistic Therapy, *ACS Nano*, 2021, **15**(12), 20643–20655.

2 Z. Zhou, J. Song, L. Nie and X. Chen, Reactive oxygen species generating systems meeting challenges of photodynamic cancer therapy, *Chem. Soc. Rev.*, 2016, **45**(23), 6597–6626.

3 N. Liu, H. Liu, H. Chen, G. Wang, H. Teng and Y. Chang, Polyphotosensitizer nanogels for GSH-responsive histone deacetylase inhibitors delivery and enhanced cancer photodynamic therapy, *Colloids Surf., B*, 2020, **188**, 110753.

4 S. Y. Chen, L. P. Zhao, Z. X. Chen, C. Y. Huang, R. J. Kong, Y. Q. Wang, D. W. Zhang, S. Y. Li, H. H. Ti and H. Cheng, Self-delivery biomedicine for enhanced photodynamic therapy by feedback promotion of tumor autophagy, *Acta Biomater.*, 2023, **158**, 599–610.

5 C. B. Simone II, J. S. Friedberg, E. Glatstein, J. P. Stevenson, D. H. Sterman, S. M. Hahn and K. A. Cengel, Photodynamic therapy for the treatment of non-small cell lung cancer, *J. Thorac. Dis.*, 2012, **4**(1), 63–75.

6 X. Yi, J. J. Hu, J. Dai, X. Lou, Z. Zhao, F. Xia and B. Z. Tang, Self-Guiding Polymeric Prodrug Micelles with Two Aggregation-Induced Emission Photosensitizers for Enhanced Chemo-Photodynamic Therapy, *ACS Nano*, 2021, **15**(2), 3026–3037.

7 X. Ai, L. Lyu, Y. Zhang, Y. Tang, J. Mu, F. Liu, Y. Zhou, Z. Zuo, G. Liu and B. Xing, Remote Regulation of Membrane Channel Activity by Site-Specific Localization of Lanthanide-Doped Upconversion Nanocrystals, *Angew. Chem.*, 2017, **56**(11), 3031–3035.

8 C. Liu, D. Wang, S. Zhang, Y. Cheng, F. Yang, Y. Xing, T. Xu, H. Dong and X. Zhang, Biodegradable Biomimic Copper/Manganese Silicate Nanospheres for Chemodynamic/Photodynamic Synergistic Therapy with Simultaneous Glutathione Depletion and Hypoxia Relief, *ACS Nano*, 2019, **13**(4), 4267–4277.

9 K. Liang, H. Sun, Z. Yang, H. Yu, J. Shen, X. Wang and H. Chen, Breaking the Redox Homeostasis: an Albumin-Based Multifunctional Nanoagent for GSH Depletion-Assisted Chemo-/Chemodynamic Combination Therapy, *Adv. Funct. Mater.*, 2021, **31**, 2100355.

10 Y. Wu, Y. Li, G. Lv and W. Bu, Redox dyshomeostasis strategy for tumor therapy based on nanomaterials chemistry, *Chem. Sci.*, 2022, **13**(8), 2202–2217.

11 Y. Liu, S. Zhai, X. Jiang, Y. Liu, K. Wang, C. Wang, M. Zhang, X. Liu and W. Bu, Intracellular Mutual Promotion of Redox Homeostasis Regulation and Iron Metabolism Disruption for Enduring Chemodynamic Therapy, *Adv. Funct. Mater.*, 2021, **31**, 2010390.

12 X. Li, L. Hetjens, N. Wolter, H. Li, X. Shi and A. Pich, Charge-reversible and biodegradable chitosan-based microgels for lysozyme-triggered release of vancomycin, *J. Adv. Res.*, 2023, **43**, 87–96.

13 X. Li, H. Sun, H. Li, C. Hu, Y. Luo, X. Shi and A. Pich, Multi-Responsive Biodegradable Cationic Nanogels for Highly Efficient Treatment of Tumors, *Adv. Funct. Mater.*, 2021, **31**, 2100227.

14 Y. Lu, Q. Luo, X. Jia, J. P. Tam, H. Yang, Y. Shen and X. Li, Multidisciplinary strategies to enhance therapeutic effects of flavonoids from Epimedii Folium: Integration of herbal medicine, enzyme engineering, and nanotechnology, *J. Pharm. Anal.*, 2023, **13**(3), 239–254.

15 D. Zhang, Y. Meng, Y. Song, P. Cui, Z. Hu and X. Zheng, Precision therapy through breaking the intracellular redox

balance with an MOF-based hydrogel intelligent nanobot for enhancing ferroptosis and activating immunotherapy, *Nanoscale*, 2022, **14**(23), 8441–8453.

16 M. Wang, M. Chang, C. Li, Q. Chen, Z. Hou, B. Xing and J. Lin, Tumor-Microenvironment-Activated Reactive Oxygen Species Amplifier for Enzymatic Cascade Cancer Starvation/Chemodynamic/Immunotherapy, *Adv. Mater.*, 2022, **34**(4), e2106010.

17 Z. Zhou, C. Zheng, Y. Liu, W. Luo, H. Deng and J. Shen, Chitosan biguanide induced mitochondrial inhibition to amplify the efficacy of oxygen-sensitive tumor therapies, *Carbohydr. Polym.*, 2022, **295**, 119878.

18 Y. Sun, X. Du, J. Liang, D. Wang, J. Zheng, Z. Bao, Z. Zhao and Y. Yuan, A multifunctional metal-organic framework nanosystem disrupts redox homeostasis for synergistic therapy, *J. Colloid Interface Sci.*, 2023, **645**, 607–617.

19 M. Chen, J. Yang, L. Zhou, X. Hu, C. Wang, K. Chai, R. Li, L. Feng, Y. Sun, C. Dong and S. Shi, Dual-Responsive and ROS-Augmented Nanoplatform for Chemo/Photodynamic/Chemodynamic Combination Therapy of Triple Negative Breast Cancer, *ACS Appl. Mater. Interfaces*, 2022, **14**(1), 57–68.

20 S. Y. Kim, S. J. Kim, B. J. Kim, S. Y. Rah, S. M. Chung, M. J. Im and U. H. Kim, Doxorubicin-induced reactive oxygen species generation and intracellular Ca^{2+} increase are reciprocally modulated in rat cardiomyocytes, *Exp. Mol. Med.*, 2006, **38**(5), 535–545.

21 T. Liu, W. Liu, M. Zhang, W. Yu, F. Gao, C. Li, S. B. Wang, J. Feng and X. Z. Zhang, Ferrous-Supply-Regeneration Nanoengineering for Cancer-Cell-Specific Ferroptosis in Combination with Imaging-Guided Photodynamic Therapy, *ACS Nano*, 2018, **12**(12), 12181–12192.

22 Y. Yang, Q. Tian, S. Wu, Y. Li, K. Yang, Y. Yan, L. Shang, A. Li and L. Zhang, Blue light-triggered Fe^{2+}-release from monodispersed ferrihydrite nanoparticles for cancer iron therapy, *Biomaterials*, 2021, **271**, 120739.

23 F. Wu, H. Chen, R. Liu, Y. Suo, Q. Li, Y. Zhang, H. Liu, Z. Cheng and Y. Chang, An active-passive strategy for enhanced synergistic photothermal-ferroptosis therapy in the NIR-I/II biowindows, *Biomater. Sci.*, 2022, **10**(4), 1104–1112.

24 Q. Liu, L. Zhou, L. Liu, J. Li, S. Wang, H. Znad and S. Liu, Magnetic ZnO@Fe_3O_4 composite for self-generated H_2O_2 toward photo-Fenton-like oxidation of nitrophenol, *Composites, Part B*, 2020, **200**, 108345.

25 W. Tao, N. Wang, J. Ruan, X. Cheng, L. Fan, P. Zhang, C. Lu, Y. Hu, C. Che, D. Sun, J. Duan and M. Zhao, Enhanced ROS-Boosted Phototherapy against Pancreatic Cancer *via* Nrf2-Mediated Stress-Defense Pathway Suppression and Ferroptosis Induction, *ACS Appl. Mater. Interfaces*, 2022, **14**(5), 6404–6416.

26 Z. Shen, T. Liu, Y. Li, J. Lau, Z. Yang, W. Fan, Z. Zhou, C. Shi, C. Ke, V. I. Bregadze, S. K. Mandal, Y. Liu, Z. Li, T. Xue, G. Zhu, J. Munasinghe, G. Niu, A. Wu and X. Chen, Fenton-Reaction-Acceleratable Magnetic Nanoparticles for Ferroptosis Therapy of Orthotopic Brain Tumors, *ACS Nano*, 2018, **12**(11), 11355–11365.

27 F. Wu, H. Chen, R. Liu, Y. Suo, Q. Li, Y. Zhang, H. Liu, Z. Cheng and Y. Chang, Modulation of the Tumor Immune Microenvironment by Bi_2Te_3-Au/Pd-Based Theranostic Nanocatalysts Enables Efficient Cancer Therapy, *Adv. Healthcare Mater.*, 2022, **11**(19), e2200809.

28 X. Meng, D. Li, L. Chen, H. He, Q. Wang, C. Hong, J. He, X. Gao, Y. Yang, B. Jiang, G. Nie, X. Yan, L. Gao and K. Fan, High-Performance Self-Cascade Pyrite Nanozymes for Apoptosis-Ferroptosis Synergistic Tumor Therapy, *ACS Nano*, 2021, **15**(3), 5735–5751.

29 A. Dong, X. Ye, J. Chen, Y. Kang, T. Gordon, J. M. Kikkawa and C. B. Murray, A generalized ligand-exchange strategy enabling sequential surface functionalization of colloidal nanocrystals, *J. Am. Chem. Soc.*, 2011, **133**(4), 998–1006.

30 X. Li, W. Diao, H. Xue, F. Wu, W. Wang, B. Jiang, J. Bai, B. Lian, W. Feng, T. Sun, W. Yu, J. Wu, M. Qu, Y. Wang and Z. Gao, Improved efficacy of doxorubicin delivery by a novel dual-ligand-modified liposome in hepatocellular carcinoma, *Cancer Lett.*, 2020, **489**, 163–173.

31 A. Pan, M. G. Jakaria, S. A. Meenach and G. D. Bothun, Radiofrequency and Near-Infrared Responsive Core-Shell Nanostructures Using Layersome Templates for Cancer Treatment, *ACS Appl. Bio Mater.*, 2020, **3**(1), 273–281.

32 Y. Chen, Y. Gao, Y. Li, K. Wang and J. Zhu, Synergistic chemo-photodynamic therapy mediated by light-activated ROS-degradable nanocarriers, *J. Mater. Chem. B*, 2019, **7**(3), 460–468.

33 M. A. Doustvandi, F. Mohammadnejad, B. Mansoori, H. Tajalli, A. Mohammadi, A. Mokhtarzadeh, E. Baghbani, V. Khaze, K. Hajiasgharzadeh, M. M. Moghaddam, M. R. Hamblin and B. Baradaran, Photodynamic therapy using zinc phthalocyanine with low dose of diode laser combined with doxorubicin is a synergistic combination therapy for human SK-MEL-3 melanoma cells, *Photodiagn. Photodyn. Ther.*, 2019, **28**, 88–97.

34 Y. Zhou, B. Zhou, L. Pache, M. Chang, A. H. Khodabakhshi, O. Tanaseichuk, C. Benner and S. K. Chanda, Metascape provides a biologist-oriented resource for the analysis of systems-level datasets, *Nat. Commun.*, 2019, **10**(1), 1523.

35 Y. Wang, L. Zheng, W. Shang, Z. Yang, T. Li, F. Liu, W. Shao, L. Lv, L. Chai, L. Qu, Q. Xu, J. Du, X. Liang, J. Zeng and J. Jia, Wnt/beta-catenin signaling confers ferroptosis resistance by targeting GPX4 in gastric cancer, *Cell Death Differ.*, 2022, **29**(11), 2190–2202.

36 M. Pertea, D. Kim, G. M. Pertea, J. T. Leek and S. L. Salzberg, Transcript-level expression analysis of RNA-seq experiments with HISAT, StringTie and Ballgown, *Nat. Protoc.*, 2016, **11**(9), 1650–1667.

37 M. I. Love, W. Huber and S. Anders, Moderated estimation of fold change and dispersion for RNA-seq data with DESeq2, *Genome Biol.*, 2014, **15**(12), 550.